A three-step process of manganese acquisition and storage in the microalga *Chlorella sorokiniana*

Snežana Vojvodić[1], Milena Dimitrijević[1], Milan Žižić[1], Tanja Dučić[2], Giuliana Aquilanti[3], Marina Stanić[1], Bernd Zechmann[4], Jelena Danilović Luković[1,5], Dalibor Stanković[6], Miloš Opačić[1], Arian Morina[1,7], Jon K. Pittman[8], Ivan Spasojević[1,*]

[1]University of Belgrade - Institute for Multidisciplinary Research, Life Sciences Department, Belgrade, Serbia
[2]CELLS-ALBA, Barcelona, Spain
[3]Elettra Sincrotrone Trieste S.C.p.A., Basovizza, Trieste, Italy
[4]Center for Microscopy and Imaging, Baylor University, Waco, TX, USA
[5]University of Belgrade, Institute for Application of Nuclear Energy, Belgrade, Serbia
[6]University of Belgrade, Faculty of Chemistry, Belgrade, Serbia
[7]Faculty of Science and Natural Resources, University Malaysia Sabah, Kota Kinabalu, Malaysia
[8]Department of Earth and Environmental Sciences, School of Natural Sciences, The University of Manchester, Manchester, UK

*Correspondence: redoxsci@gmail.com

E-mail addresses of all SV: snezanavojvodic@gmail.com; MS: mendzi.m@gmail.com; MŽ: mzizic@imsi.rs; TD: tducic@cells.es; GA: giuliana.aquilanti@elettra.eu; MS: modesty_23@yahoo.com; BZ: Bernd_Zechmann@baylor.edu; JDL: reginadelphy@yahoo.com; DS: dalibors@chem.bg.ac.rs; MO: paseportu@gmail.com; AM: arian_morina@yahoo.com; JKP: jon.pittman@manchester.ac.uk

Highlight

Manganese ions first bind to phosphate moieties in membrane and mucilage, then to intracellular polyphosphates, and finally accumulate in the microalgal cell in the form of multi-valent Mn-O-Ca clusters.

Abstract

Metabolism of metals in microalgae and the adaptation to metal excess are of significant environmental importance. We report here a three-step mechanism that the green microalga *Chlorella sorokiniana* activates during the acquisition of and adaptation to manganese (Mn), which is both, an essential trace metal and a pollutant of waters. In the early stage, Mn^{2+} was mainly bound to membrane phospholipids and phosphates in released mucilage. The outer cell wall was reorganized, and lipids were accumulated with a relative increase in lipid saturation. Intracellular redox settings were rapidly altered in the presence of Mn excess, with increased production of reactive oxygen species that resulted in lipid peroxidation and a decrease in the level of thiols. In the later stage, Mn^{2+} was chelated by polyphosphates and accumulated in the cells. The structure of the inner cell wall was modified and the redox milieu established a new balance. Polyphosphates serve as a transient Mn^{2+} storage ligand, as proposed previously. At the final stage, Mn was stored in multi-valent Mn clusters that resemble the structure of tetramanganese-calcium core of the oxygen-evolving complex. The present findings elucidate bioinorganic chemistry and metabolism of Mn in microalgae, and may shed new light on water-splitting Mn clusters.

Keywords: *cluster; ligand; metals; microalgae; oxidative stress; polyphosphates; XAFS*

Introduction

Manganese (Mn) serves as a co-factor of more than 30 enzymes in microalgae, including two of the core components of energy and redox metabolism – the oxygen evolving complex (OEC) in Photosystem II (PSII), and Mn superoxide dismutase (Liu *et al.*, 2018). As a consequence, microalgal cells require significant quotas of Mn for normal function during growth (Tsednee *et al.*, 2019). However, Mn shows limited availability in some waters with a negative consequence on microalgal productivity (Liu *et al.*, 2018). In addition, the metabolism of Mn appears to be intertwined with iron (Fe), which is the key limiting metal nutrient for microalgae in most aquatic ecosystems (Hanikenne *et al.*, 2021). On the other hand, Mn is a common pollutant from anthropogenic sources, such as mining and industrial drainage, and from natural deposits of Mn oxides that are reduced to Mn^{2+}, the main redox form in water at pH < 8 (Röllin and Nogueira, 2019). Many microalgal species can tolerate metal excess and microalgal communities may act opportunistically to accumulate metals if they are present in abundance, particularly Mn and Fe. Therefore, the exposure of microalgae to high but non-toxic concentrations of metals represents a powerful tool in the analysis of metal metabolism (Tsednee *et al.*, 2019; Schmollinger *et al.*, 2021). In addition, the capability of microalgae to act as pioneers of inhospitable mining wastewaters holds a promise of development of microalgae-based biotechnologies for efficient and cost-effective wastewater processing and metal recovery (Malavasi *et al.*, 2020). The elucidation of adaptive mechanisms that microalgae employ to mitigate Mn excess is essential for bioengineering of organisms with improved remediation performances.

The aim of this study was to establish the mechanisms of Mn interactions with the freshwater green microalga *Chlorella sorokiniana*. Recent studies have shed light on some of the mechanisms of Mn metabolism of *Chlamydomonas reinhardtii*. It has been pinpointed that the response to Mn is a dynamic process and that polyphosphates are important but not the final Mn storage ligands (Tsednee *et al.*, 2019; Schmollinger *et al.*, 2021). Additional or alternative mechanisms are possible due to the rich bioinorganic and redox chemistry of Mn (Cotton *et al.*, 1999). The *Chlorella* genus shows huge environmental and biotechnological importance in relation to the tolerance to heavy pollution and the efficiency of CO_2 fixation (Krichen *et al.*, 2019). In the present study, several aspects of the response to a high but non-toxic Mn treatment were analyzed using a broad set of methods. Changes in structure and chemical composition of microalgal cells were analyzed using scanning electron microscopy (SEM) with energy dispersive X-ray spectrometry (EDS), and synchrotron radiation-based Fourier transform mid-infrared spectroscopy (SR-FTIR). Intracellular redox changes were assessed by assays for production of reactive oxygen species (ROS), oxidation of thiols, and total glutathione levels. Finally, redox and coordination chemistry of Mn in microalgae were analyzed using electron paramagnetic resonance (EPR) spectroscopy, cyclic voltammetry, and X-ray absorption fine structure (XAFS) spectroscopy, including X-ray absorption near edge structure (XANES) and extended X-ray absorption fine structure (EXAFS). These approaches provided an improved molecular-level understanding of Mn metabolism.

Materials and methods

Cell cultivation and treatment

C. sorokiniana strain CCAP 211/8K was obtained from the Culture Collection of Algae and Protozoa (CCAP), U.K. Microalgal inocula were added to 150 mL of 3N-BBM+V medium in 250 mL Erlenmeyer flasks at the initial density of 0.5×10^6 cells/mL. 3N-BBM+V medium was prepared according to the CCAP recipe (Culture Collection of Algae and Protozoa, 2022). The initial pH of the medium was ~7.5. Microalgae cultures were grown at 22°C on orbital shakers (120 rpm) in a growth cabinet with a continuous photon flux of 120 µmol m^{-2} s^{-1} (MST TL-D Reflex 36W840 1 SLV/25 tubes, Philips, Amsterdam, The Netherlands). Flasks with samples were weighed on day 0 and the volume of samples was corrected for evaporation at day 15 with sterile deionized water. The growth was monitored using optical density at 750 nm (OD_{750}), which is proportional to cell density. Microalgae were exposed to $MnCl_2$ at day 7 (exponential phase of growth), or at day 20 (early stationary or late exponential phase), with the following total concentrations of Mn: 0.1, 1, 5, 10, and 20 mM. The response of the cultures to $MnCl_2$ were examined by measuring OD_{750} at 1 h, 1 day, 2 days, and 7 days of treatment. Furthermore, microalgae cells in the two phases of growth were compared according to their capacity to accumulate Mn. OD_{750} of cultures at day 20 were adjusted to the average OD_{750} in cultures at day 7 to normalize against differences in cell number. Samples were exposed to 1 mM $MnCl_2$ for 24 h. Biomass was washed 3× with water and digested. The concentration of Mn in the biomass was established using inductively coupled plasma - atomic emission spectroscopy (ICP-AES) on an Avio 200 spectrometer (PerkinElmer, Waltham, MA, U.S.A.) and Mn emission line at 257.610 nm. The results were expressed as the amount of Mn per g of dry biomass. For biomass determination, 2 mL aliquots of cultures were centrifuged at 5000 g/5 min, and the cell pellet was left to dry for 24 h at 60°C and then weighed. In addition, the kinetics of Mn accumulation in the cells and the changes in concentrations of other essential elements including Fe (emission line at 238.204 nm), zinc (Zn; 206.200 nm), and phosphorus (P; 213.617 nm) were analyzed over a duration of 72 h in day 20 cultures that were treated with 1 mM $MnCl_2$, using the same ICP-AES protocol. Next, changes in biomass were determined for microalgae treated at day 20. Cell viability was evaluated in early stationary phase cultures during the period of 7 days (starting at day 20) using the Evans Blue stain, as described previously (Zuppini *et al.*, 2007). The goal was to determine if observed changes in the stationary phase are potentially related to an increased number of dead cells during the treatment period. Of note, non-viable cells show disrupted membranes that allow accumulation of Evans Blue dye in the cell. The viability is presented as % of Evans Blue negative cells. At least 100 cells were analyzed per sample. All further treatments were performed at day 20 of culture growth. All treatments were performed in the 3N-BBM+V medium. All chemicals were acquired from Sigma–Aldrich (St. Louis, MI, U.S.A.).

SEM with EDS

Microalgae samples (1.5 mL) were left untreated or treated with 1 mM $MnCl_2$ for 15 min, 1 h or 24 h, washed once with the growth medium with no added vitamins, and collected for further analysis. Cells were spun at 5000 g/5 min. Fixation was performed as described previously (Vojvodić *et al.*, 2020a). Samples were critical point dried (CPD300, Leica Microsystems, Wetzlar, Germany), sputter coated with carbon (ACE600, Leica Microsystems), and examined by SEM (Versa 3D, FEI/Thermo Fisher, Hillsboro, OR, U.S.A.). EDS was performed with an Octane Pro silicon drift detector

(EDAX/AMTEK, Mahwah, NJ, U.S.A.) at 20 kV, and a working distance of 10 mm. According to Monte Carlo simulation, EDS detected Mn specific X-ray signals from up to 2.4 µm of biomass depth with an x/y resolution of 1.6 µm. EDS results were presented as atomic fractions - the percentage of moles of an element in the total number of moles in the sample. It is important to note that EDS delivered information on the atomic composition of mucilage, the cell wall, and some intracellular space, since the beam penetrated ~2.4 µm, whereas the diameter of *C. sorokiniana* cells is 3–4 µm.

SR-FTIR

The FTIR spectroscopy measurements were performed at the MIRAS Beamline at ALBA Synchrotron (Barcelona, Spain). Microalgal samples (150 mL) were untreated, or treated with 1 mM $MnCl_2$ for 1 h and 24 h. Cells were spun down at 5000 g/5 min, washed 3× with water (50 mL), and freeze-dried. Spectra were obtained from three biological replicates of control and treated microalgae. A total of 90-120 independent spectra were accumulated from different points in the samples and averaged to produce representative spectra. The spectra were analyzed for the main bio-molecular families: carbohydrates and nucleic acids (1480–900 cm^{-1}), proteins (1790–1480 cm^{-1}), and lipids (3030–2800 cm^{-1}). The assignment of bands was performed according to available literature (Derenne *et al.*, 2013; Driver *et al.*, 2015; Wiercigroch *et al.*, 2017). In addition, spectra were processed using extended multiplicative signal correction (EMSC2) (Martens and Stark, 1991), that included baseline correction, then first analyzed by principal components analysis using the NIPALS algorithm. This was then followed by discriminant function analysis (DFA), which discriminated the groups on the basis of retained principal components. All statistical calculations were performed using a DFA algorithm in MATLAB v.R2019a (MathWorks, Natick, MA, U.S.A.). SR-FTIR data were used to measure two parameters that reflect the oxidative status: (i) the relative level of C=C bonds (*i.e.* unsaturation in lipids) that was established from the intensity of a band at 3002 cm^{-1} (C=C–H stretching in unsaturated lipids); and (ii) CH_2/CH_3 ratio (the compositional saturation index), which was established according to asymmetric stretching vibrations of these groups that occur at 2920 and 2960 cm^{-1}. A decrease of C=C levels and CH_2/CH_3 ratio reflects increased lipid peroxidation (Borchman and Sinha, 2002). Lipid peroxidation breaks double bonds. CH_2/CH_3 ratio is influenced primarily by the degree of saturation of the fatty acids, and therefore a drop implies oxidative damage of fatty acid chains that results in the loss of double bonds, so that CH moieties turn into CH_2.

Intracellular level of oxidizing species

Intracellular amount of ROS was evaluated using dichlorodihydrofluorescein diacetate (DCFH-DA), a cell-permeable probe, which is hydrolyzed to DCFH carboxylate anion and retained in the cell. Two-electron oxidation of DCFH by hydrogen peroxide and other oxidants results in the formation of a fluorescent product, dichlorofluorescein (DCF), which reflects redox conditions in the cell (Kalyanaraman *et al.*, 2012). Aliquots were collected at different time points from untreated cultures or cultures exposed to 1 mM $MnCl_2$, washed 2× with water, and diluted with water to reach OD_{750} of ~0.5. DCFH-DA was dissolved in 96% ethanol and added to a final concentration of 20 µM (final ethanol concentration was 1%). Samples were incubated in the dark for 20 min at 25°C. Samples (200 µL) were placed in microtiter plates (black/clear bottom), and DCF fluorescence with excitation/emission at 485/530 nm was read on a Tecan Infinite M Nano microplate reader (Tecan Group Ltd, Männedorf, Switzerland). The results are presented as DCF fluorescence intensity (in

arbitrary units) of the sample reduced by autofluorescence of microalgae and fluorescence of DCFH-DA (20 µM) + $MnCl_2$ (1 mM).

Total concentration of free glutathione

Samples were prepared as for the FTIR experiments, and further processed as previously described (Rijstenbil *et al.*, 1998). In brief, freeze-dried samples (5 mg) were re-suspended in 250 µL of extraction buffer (5% 5-sulfosalicylic acid + 6.3 mM diethylenetriaminepentaacetic acid; pH 2), snap frozen in liquid N_2, and homogenized in a ball mill at 30 Hz, 4 × 15 s, with freezing in liquid N_2 between cycles. Samples were incubated for 10 min on ice, and then centrifuged at 12000 g/20 min/0^{o}C. The total concentration of glutathione (reduced + oxidized) was measured using Ellman's reagent that reacts with reduced thiols to give a colored product and the reduction of oxidized thiols, according to a previously described protocol (Rahman *et al.*, 2006). It is important to note that 5% 5-sulfosalicylic acid induces precipitation of proteins to remove protein thiol groups from the samples, and this also removes bound glutathione.

EPR spectroscopy – assay for reduced thiols

X-band EPR spectroscopy was applied to establish the concentration of reduced thiol groups in live microalgae using the disulfide biradical (RSSR) method (Khramtsov *et al.*, 1989). Disulfide bonds are split in the reaction of RSSR with thiols, resulting in characteristic changes of the EPR spectra that are quantified. A stock solution of RSSR (2 mM) was prepared in DMSO. Aliquots were collected at different time points from untreated cultures or cultures exposed to 1 mM $MnCl_2$, washed once with water, and placed in water to reach the number of approximately 2 × 10^6 cells in 50 µL samples. The samples were incubated for 10 min with RSSR (100 µM final concentration), and EPR spectra were recorded on a Bruker EMX Nano X-band (9.65 GHz) spectrometer (Bruker, Billerica, MA, U.S.A.), with the following settings: attenuation, 20 dB; modulation amplitude, 0.1 mT; modulation frequency, 100 kHz; scan time, 60 s; room temperature (RT). A calibration curve was built using a set of different concentrations of reduced glutathione in the 10-100 µM range, according to the relative increase of the amplitude of the first peak of the EPR signal. The relative increase was calculated as follows: $(I - I_0)/I_0$ (I – amplitude in the presence of thiols; I_0 amplitude in the absence of the thiols).

EPR spectroscopy of Mn

Microalgal cultures were exposed to 1 mM $MnCl_2$ for 1 h or 24 h, spun down at 5000 g/5 min and washed once with the same volume of medium, after which samples were divided into two parts. One part was washed 3× with water (50 mL), and the other was washed 3× with 20 mM extracellular chelating agent ethylenediaminetetraacetic acid (EDTA) solution (50 mL), to remove Mn^{2+} that was bound to the cell surface. Cells were snap frozen and freeze-dried overnight. Samples (10–15 mg) were placed into quartz tubes, and EPR measurements were performed on a Bruker EMX Nano spectrometer, using the following settings: power attenuation, 20 dB; modulation amplitude, 0.6 mT; modulation frequency, 100 kHz; scan time, 120 s; RT. Spectra were normalized to dry biomass.

Cyclic voltammetry

Samples (150 mL) were untreated or treated with $MnCl_2$ (1 mM) for 1 h, 24 h, and 48 h. Cells were spun down and washed 3× with water (50 mL) at 5000 g/5 min, freeze-dried, and powdered in liquid N_2. Samples were resuspended in 5% (v/v) nitric acid (0.5 mg of biomass/mL), and vortexed for 1 min. Nitric acid is commonly used in elution and recovery of metal ions (Alomar *et al.*, 2021).

Measurements were performed at RT, immediately after sample preparation. Standard solutions (1 mM) of $MnCl_2$, MnO_2, Mn_2O_3, and $KMnO_4$ were also prepared in 5% nitric acid (Mn_2O_3 was not fully dissolved). Electrochemical measurements were performed on a potentiostat/galvanostat CHI 760b (CH Instruments, Austin, TX, U.S.A.), using a conventional three electrode cell. The electrodes used were a platinum working electrode (model CHI 102, CH Instruments), an Ag/AgCl (3 M KCl) reference electrode (model CHI 111, CH Instruments), and a platinum wire auxiliary electrode (model CHI 115, CH Instruments).

XAFS

Cell cultures (150 mL) were untreated or exposed to 1 mM $MnCl_2$ for 1 h, 24 h or 72 h. Cells were spun down at 5000 g/5 min and washed 3× with medium (50 mL). Samples were freeze-dried and powdered. XANES and EXAFS experiments were performed on the XAFS beamline at the Elettra synchrotron facility. The spectra were collected in transmission mode at RT, with an energy step of 5 eV in the pre-edge region, 0.2 eV in the edge region, and $\Delta k = 0.03$ Å $^{-1}$ at higher energies. The electron storage ring provided energy of 2.0 GeV. XANES spectra of reference standards of Mn in 2+, 3+, 4+ and 7+ oxidation states ($MnCl_2$, Mn-acetate, Mn_2O_3, Mn_3O_4, MnO_2, $KMnO_4$) were collected to estimate oxidation states and coordination environments of Mn in the cells, directly or by making their linear combinations. All spectra were collected in triplicate, normalized and merged to improve signal to noise ratio. The XANES analysis was carried out using the ATHENA software package (Ravel and Newville, 2005). FEFF software (University of Washington) was used for *ab initio* multiple scattering calculations of EXAFS spectra. Fits of k^3-weighted EXAFS oscillations were performed for k values ranging from 2 to 16 $Å^{-1}$. Structural parameters were obtained without the phase corrections, by fitting the data in the R-space, within the interval of 1–3.4 Å. All calculated distances were within 0.05 Å of the used model. Edge energy values were in the range of 0–1 eV, and mean-square radial displacements were lower than 0.01 $Å^2$. FEFF simulation is a method that calculates interatomic distances in molecules and clusters according to the crystallographic data obtained from COD database (http://www.crystallography.net/cod/) and EXAFS spectra of compounds that are available in the literature. In order for the resulting crystallographic model to be considered as an appropriate match with experimental data, several parameters must be met: distance deviation from the model has to be < 0.1 Å; E_0 must be within the limits of 3 eV compared to the sample E_0; reduction factor have to be between 0.7 and 1; and Debye-Waller factor has to be positive and not to overpass departure of 0.03 from the model. The relative contributions of compounds with different Mn oxidation states and coordination environments to the 72 h sample were established for the energy range between -20 eV and +30 eV relative to energy of E_0 (energy necessary to eject the electron from the first shell), using linear combination fitting in ATHENA.

Statistics

All experiments were performed with at least three biological replicates. Results are presented as mean values ± standard error (SE) of the mean. The results of fitting in ATHENA are presented as a relative contribution of different Mn species (%) in the the optimal fit with standard deviations. Lipid peroxidation data are presented as box plots. Statistical significance ($p < 0.05$) was calculated using Mann–Whitney 2-tailed test or one-way ANOVA followed by Duncan's *post hoc* test. Correlation analysis was performed using Spearman's rank correlation coefficients (R). Data were considered statistically significant for $p < 0.05$.

Results and discussion

Mn excess induces mucilage release, accumulation of phosphates, and changes in the composition of bio-molecules

The first step in this study was to establish the upper limit of non-toxic Mn^{2+} concentration range for the *C. sorokiniana* cells. The effects of different concentrations of Mn^{2+} were tested in the exponential phase and in the early stationary phase of culture growth (Fig. 1A). A gradual and significant increase of cell density as determined by OD_{750} measurement was observed during both growth phases in control cultures and in cultures treated with Mn^{2+} at concentrations < 5 mM (Fig. 1B and C). The concentration of 5 mM Mn^{2+} showed negative effects in the early stationary phase, while 10 and 20 mM stopped the cell growth regardless of the phase of growth. The negative effects of high Mn^{2+} concentrations on microalgae growth in the early stationary phase was confirmed by biomass changes (Fig. 1D). In accord with these results, all further experiments were performed using 1 mM Mn^{2+}. This concentration is 'safely' within the non-toxic range, although it is high compared to natural levels in typical freshwaters (World Health Organization, 2011). It is noteworthy that toxic effects of Mn^{2+} excess in microalgae have been related to mis-metallation – the replacement of metals in active centers of metalloproteins with Mn, and to redox perturbations (Eisenhut, 2019). The similarity of the response to Mn in different phases was further implicated by similar amounts of Mn accumulation, which were not significantly different (Fig. 1E). Pertinent to this, we analyzed the interactions of microalgae with Mn^{2+} in the early stationary phase, taking into account that Mn accumulation in *Chlamydomonas reinhardtii* has been shown to mainly take place when cells transitioned to the stationary phase (Tsednee *et al.*, 2019). The same study has reported drastic changes in Mn coordination after ~48 h treatment with Mn^{2+} excess. In line with this, the timeframe of the current study was set at 72 h following Mn addition. Importantly, the viability of untreated cell cultures in the early stationary phase did not decrease significantly during 72 h from the day 20 time point (Fig. 1F). This implies that the effects of Mn^{2+} during this period were not significantly affected by a background of cell death within the population.

Microalgal cells started releasing mucilage polymers between 15 min and 1 h of exposure to Mn^{2+} at day 20 and accumulated the mucilage on the surface of the cells during 24 h after treatment (Fig. 2A). Mucilage represents a complex amorphous adhesive matrix that is immersed in the surrounding fluid (Watanabe *et al.*, 2006). Strains from the *Chlorella* genus release a soluble type of mucilage which is predominately composed of polysaccharides (Naveed *et al.*, 2019). The building components of mucilage polysaccharides in *C. sorokiniana* are (in order according to their fraction in biomass): sucrose, galacuronic acid, xylitol, inositol, ribose, mannose, arabinose, galactose, and rhamnose (Watanabe *et al.*, 2006). It is important to point out that the exposure of microalgal cells to high but non-toxic Mn^{2+} concentrations allows the acquisition of a physiological quota and opportunistic accumulation of this essential metal, but may also induce an adaptive response for metal tolerance (Tsednee *et al.*, 2019). Mucilage and cell wall polymers regulate the chemical milieu surrounding the cell, serving as both a sink for metal storage and as a barrier against metal excess (Sutak *et al.*, 2012; Naveed *et al.*, 2019). The release of mucilage in this study is probably more a means of protection against uncontrolled diffusion of Mn into the cells. It appears that the response of *C. sorokiniana* to Mn^{2+} was slower than the response to equimolar Cu^{2+} that we have reported previously (Vojvodić *et al.*, 2020a). This is in line with the general higher sensitivity of microalgae to

Cu than Mn (Tsednee *et al.*, 2019). Atomic fractions of elements in the biomass were drastically altered at 24 h: the O fraction showed a two-fold increase (+10%); the P fraction was increased almost three-fold (from 0.6% in untreated control to 1.5%); and, as a consequence, the C fraction dropped by ~12% (Fig. 2B). The observed rise in the atomic fractions of both O and P after 24 h implies that microalgae accumulate phosphates from the medium via polymerization. Polyphosphates can be stored within cells or they may be bound to the cell wall and mucilage (Oh-hama *et al.*, 1986).

Measurement of Mn accumulation over time showed that Mn initially accumulates rapidly within the first hour after Mn addition to a concentration just below 10 mg/g then remained at an equivalent concentration for the next 24 h (Fig. 2C). The concentration of Mn the medium at day 20 was 7.6 ± 0.7 µg/L. After 24 h the Mn level steadily increased three- to four-fold to a concentration of approximately 25 – 30 mg/g by the 72 h time point. This demonstrates that significant accumulation of Mn takes place in the later stage of the response. Besides the uptake of Mn by Mn^{2+} transporters, such as members of the ZIP transporter family, Mn^{2+} may enter microalgal cells via phosphate transporters - as $MnHPO_4$ or as a counter-ion (Blaby-Haas and Merchant, 2012), or through non-selective cation channels and Ca^{2+}-permeable channels, which are generally permeable to Mn^{2+} (Alejandro *et al.*, 2020). Total P showed a similar profile to that of Mn (Fig. 2C), such that there was a significant positive correlation between Mn and P (R = 0.936). In contrast, there was no significant change in Fe concentration over time in response to Mn addition. Likewise, there was no significant change in Zn concentration over 48 h but by 72 h Zn content was below detectable limits (Fig. 2C). As such there was a significant negative correlation between Mn and Zn (R = -0.433), perhaps suggesting some evidence of mis-metallation between Mn and Zn. This may also be evidence of competition between Zn and Mn uptake, in line with previous observations in green algae that these metals share plasma membrane transport pathways (Sunda and Huntsman, 1998).

Changes in the composition of bio-molecules following Mn exposure were further examined using SR-FTIR (Fig. 2D-2F; Supplementary Fig. S1; Supplementary Fig. S2). SR-FTIR shows very high sensitivity and resolution in providing information on different chemical groups (Table 1). There were several important changes in the carbohydrate and phosphate 'fingerprint' region (Fig. 2D). The 1248 cm^{-1} band was shifted to a lower wavenumber after 1 h of Mn exposure. This can be explained by the binding of Mn^{2+} to phosphate groups on membrane phospholipids, which results in longer and weaker bonds. The change was reversed after 24 h, which means that the interaction took place transiently during the early stage of the response. Bands at 1184 cm^{-1} and 940 cm^{-1} emerged after 24 h. This implicates alterations in carbohydrate chains. In addition, the amplitudes of bands deriving from bending vibrations of CH_2 groups (1448 and 1378 cm^{-1}) were decreased, whereas the 1149 cm^{-1} and 1072 cm^{-1} bands were increased after 24 h (Supplementary Fig. S1). This implicates a change in carbohydrate profile in the later stage of the response. The change may be related to the accumulation of mucilage, or to structural alterations in the inner fibrilar cell wall, which in *C. sorokiniana*, is composed of rhamnose, galactose, glucuronic acid, arabinose, mannose, and other sugars (Russell, 1995). Next, the exposure to Mn^{2+} induced a shift to higher energy of the 1644 cm^{-1} band (Fig. 2E and Supplementary Fig. S1), which was assigned to the stretching vibration of C=O···H-N structure in primary amides. In addition to proteins, amide groups in *Chlorella* biomass are present in chitosan-like polymers that make the outer 'rigid' cell wall (Baudelet *et al.*, 2017). It has been shown previously that the strength of the hydrogen bond in C=O···H-N structure is increased when chitosan is more tightly packed, or when a nearby uncharged ligand groups

coordinate to metals, including Mn^{2+} (Husberg and Ryde, 2013). Therefore, the observed shift implicates restructuring of proteins and the outer cell wall or the binding of Mn^{2+} to the cell wall.

SR-FTIR of lipids showed the most conspicuous changes (Fig. 2F). The increase in amplitudes of the asymmetric stretching bands of CH_3 and CH_2 at 1 h, and the symmetric stretching bands of CH_3 and CH_2 at 24 h imply that *C. sorokiniana* cells may accumulate lipids in response to Mn^{2+} excess and that changes in the organization or composition of lipids took place. This is in accord with previous findings that metal-induced stress may lead to lipid accumulation in microalgae (Battah *et al.*, 2015). Furthermore, CH_2 stretching bands at 2912 cm^{-1} and 2847 cm^{-1} were shifted to higher wavenumbers in the presence of Mn^{2+} after 1 h. This is strongly related to a decrease in the conformational order of the acyl chains in membranes (Boncheva *et al.*, 2008), which may be induced by Mn^{2+} interactions with the membrane. The impact of Mn^{2+} on the membrane is different than other transition metal ions, such as Cu^{2+}, Zn^{2+}, Ni^{2+}, which bind to the membrane to increase its order (Sule *et al.*, 2020). It has been reported that Mn^{2+} induces structural changes of the lipid bilayer, which has been related to membrane fluidity. The fluidity is changed by Mn^{2+} because small ionic radius allows it to bypass the polar heads and to access the phosphate moieties (Suwalsky *et al.*, 2010). Changes in membrane fluidity may affect the function of ion channels, such as mechanosensitive channels of large-conductance that are present in microalgae, to facilitate the influx of metal ions (Min *et al.*, 2014). The shift of the 1248 cm^{-1} band also speaks in favor of the binding of Mn^{2+} to phosphate groups on membrane lipids. The changes were reversed at 24 h, implying that Mn^{2+} was sequestrated/removed from the membrane in the later stage of the response. A multivariate analysis of the SR-FTIR spectral data by DFA also showed the clear shift in profile of spectra from the 1 h Mn^{2+} treatment in comparison to the control and 24 h treatment, for each of the fingerprint regions and across the full wavenumber range (Supplementary Fig. S2). DFA implicates that Mn^{2+} induces metabolic dysregulation after 1 h, and that a new metabolic balance is established after 24 h.

Intracellular redox milieu shows dynamic changes and reaches new balance

The changes in the intracellular levels of ROS and oxidation makers showed interdependent timelines in microalgae exposed to Mn^{2+} (Fig. 3). The ROS level showed two increases - within the first 15 min and between 1 h and 2 h of the Mn^{2+} exposure (Fig. 3A). At 2 h, ROS concentration reached a plateau that was kept until 24 h. The plateau level was about seven-fold higher than before the treatment and three-fold higher than at 1 h. ROS levels in untreated microalgae showed a subtle increase only at the 24 h time point. The intracellular level of reduced thiols showed dropped in concentration at 30 min and at 2 h (Fig. 3B), which followed the rise of ROS level because of ROS-induced oxidation of thiols. At 24 h, the concentration of reduced thiols returned to the baseline value. In control samples, no significant changes were observed during the 24 h period. Therefore, the vast majority of the observed increase in ROS and thiol oxidation is due to Mn^{2+} addition rather than other causes. This is important to underline, taking into account that pronounced ROS production and oxidation could be related to senescence and cell death in some aging cultures (Pérez-Pérez *et al.*, 2012). Furthermore, the total concentration of glutathione, which is the key redox buffer in microalgae (Balzano *et al.*, 2020), showed a drop at 1 h and then returned to baseline level at 24 h (Fig. 3C). The drop may be caused by the synthesis of phytochelatins (oligomers of glutathione), glutathionylation of proteins, or glutathione degradation (Balzano *et al.*, 2020). Phytochelatin synthesis is the most plausible explanation taking into account that phytochelatins represent a common component of response mechanisms of microalgae to metal excess. On the

other hand, glutathionylation or glutathione degradation would probably result in a drop in reduced thiols at 1 h, which was not the case (Fig. 3B). Finally, two markers of lipid peroxidation that were derived from SR-FTIR data showed the development of oxidative damage at 1 h of treatment, which was partially reversed at 24 h (Fig. 3D). Altogether, this implies that the applied concentration of Mn^{2+} caused an oxidative burst that the cells were able to fend off. The pro-oxidative changes, which come as a consequence of Mn influx rapidly within the first few minutes that then remained stable for 24 h, may represent a sub-toxic episode in the adaptation or opportunistic accumulation of this essential metal. Alternatively, ROS production may have a more active and sophisticated role in Mn acquisition through redox signalling and targeted/localized oxidation. For example, it has been reported that oxidative stress may promote polyphosphate synthesis (Dai *et al.*, 2021). Further, previously proposed mechanisms of Mn^{2+}-related oxidative stress involve increased production of the superoxide radical anion (superoxide) in mitochondria due to complex I inhibition, and increased production of superoxide and/or singlet oxygen in chloroplasts due to interference with PSII OEC (Rajpoot *et al.*, 2021). The reduction potential of the Mn^{3+}/Mn^{2+} pair at pH 7 is 830 mV, so Mn^{2+} is not susceptible to oxidation by superoxide. However, protonated superoxide (hydroperoxyl radical) shows higher reduction potential and may cause the oxidation of Mn^{2+} (Chaput *et al.*, 2019). Therefore, ROS may alter the redox chemistry of Mn in the cytoplasm or in specific organelles. It is noteworthy that Mn in the form of insoluble MnO_2 also induced pro-oxidative changes and lipid peroxidation in *Chlorella*, although on a much slower time scale than Mn^{2+} (Khalifeh *et al.*, 2022). A dynamic redox response has been reported previously in microalgae exposed to different other metals (Nowicka, 2022).

Mn changes redox forms and ligands in time-dependent manner

Next we analyzed the timeline of changes in the coordination and redox form of Mn in microalgal cells. EPR was applied to evaluate loose binding of Mn^{2+} to microalgal cells. Strongly bound Mn^{2+} is not detectable by EPR due to zero field splitting anisotropy that is promoted by the loss of rapid molecular tumbling in combination with a large number of transitions (Vojvodić *et al.*, 2020b). Mn^{3+} and Mn^{4+} could not be detected using EPR settings applied here. In cells treated with Mn for 1 h, a strong six-line spectrum that is characteristic for Mn^{2+} (S = 5/2, I = 5/2), was observed (Fig. 4A). Mn^{2+} signal was not present after the cells were washed with the extracellular metal-chelating agent EDTA. The signal of Mn^{2+} was weaker after 24 h than 1 h. This implies that in the early stage, Mn^{2+} is loosely bound to the cell surface, and that subsequently other stronger ligands are present. To determine the changes in the redox form of Mn in microalgal cells, we extracted Mn ions from the biomass using 5% nitric acid and performed cyclic voltammetry analysis (Fig. 4B). Voltammograms were compared to the voltammograms of standard compounds with different Mn redox forms (Fig. 4C). Mn^{2+} showed a broad oxidation peak at E_{pa} = 950 mV (oxidation to Mn^{4+} and Mn^{3+}), and two reduction peaks with E_{pc} at 285 mV and 125 mV. According to voltammograms of Mn_2O_3 and MnO_2, the peak at E_{pc} = 285 mV comes from the reduction of Mn^{3+}, whereas the peak at E_{pc} = 125 mV comes from the reduction of Mn^{4+}. Mn^{7+} showed a distinctive reduction peak at E_{pc} = 690 mV that was not detected in biomass extracts. The redox form of Mn in the biomass changed with time. After 1 h, voltammogram showed weak peak currents at potentials that are characteristic for Mn^{2+}. At 24 h, Mn^{2+} currents were much stronger, which is in line with Mn accumulation in microalgal cells that was shown by EDS. At 48 h, a drastic change took place. A strong reduction current emerged at E_{pc} = 155 mV, and the broad oxidation peak was shifted to E_{pa} = 1020 mV. Altogether this implies that in

the early stage of the Mn response, microalgae store Mn as Mn^{2+}, and then later, Mn accumulates in other complex redox/coordinate forms that involves both Mn^{3+} and Mn^{4+}.

We used XANES and EXAFS to further examine redox forms and structural properties of Mn in microalgal cells treated with $MnCl_2$. The treatment was extended to 72 h to identify the final ligands. XANES spectra of the 1 h and 24 h samples shared very similar features, with little variation in the post-edge region (Fig. 5A). Spectra differed from the $MnCl_2$ spectrum due to changes in the local geometry of the absorber without any indication that the oxidation state was changed. A comparison with XANES spectra of standard compounds pointed to the high similarity with Mn-acetate which is characterized by six O atoms in the first coordination sphere (Fig. 5B). Similar pre-edge features were present for 1 h and 24 h samples. This implies that Mn^{2+} remains in octahedral geometry. However, the pre-edge peak of the 1 h sample was more prominent and narrower than the 24 h sample (Fig. 5C). This implicates a distorted geometry in the 1 h sample and a more regular geometry in the 24 h sample. The XANES spectrum of Mn in microalgae that were treated for 72 h was strikingly different than the spectra of the 1 h and 24 h samples (Fig. 5A). The edge of the 72 h spectrum was shifted towards higher energies suggesting oxidation of Mn^{2+}. This spectrum corresponded to the fit that represents a linear combination of spectra of standard compounds: Mn_2O_3 49.4 % (with standard deviation of 5%); Mn_3O_4 27.2 % (3.6 %); MnO_2 3.8 % (3.4 %); and Mn-acetate 19.5 % (7.3 %) (Fig. 5D). All components of the fit indicate that O is the closest atom in the ligands, which excluded the possibility of a significant impact of atomic electronegativity on the position of the edge in the spectrum. The first derivatives of XANES spectra further proves the presence of Mn^{2+}, Mn^{3+}, and Mn^{4+} in the 72 h sample (Fig. 5E). Binding to O ligands is in accord with 'Hard and Soft Acids and Bases' principle. Mn^{2+}, Mn^{3+} and Mn^{4+} are hard acids and prefer O ligands, which are hard bases (Martell and Hancock, 1996).

The contribution of different oxidation forms of Mn was further examined by EXAFS (Fig. 5F). EXAFS analysis extended XANES-based information on the coordination characteristics of Mn^{2+} in the 1 h and 24 h samples. The comparison of EXAFS in R-space for the 1 h and 24 h samples gives very similar local environments with slightly different distances between Mn^{2+} and its first neighbors. According to FEFF calculations, Mn^{2+} complexes showed a octahedral environment with six O atoms in the first shell and P at higher distances in four ligands; two other ligands were water molecules (Zhang *et al.*, 2009; Elboulali *et al.*, 2013). In the 1 h sample, O atoms were closer to Mn (2.097 Å (2 O atoms), 2.139 Å (2 O), 2.192 Å (2 O)), than in the 24 h sample (2.121 Å (2 O), 2.169 Å (4 O)). The distances in the 1 h sample showed more deviation from the corresponding model (of note, deviations were never > 0.1 Å). This indicates higher distortion and accounts for higher intensity of pre-edge peak in XANES spectrum of the 1 h sample (Fig. 5C). Pertinent to this, a distorted octahedral metal environment has been reported previously for Mn^{2+} complexes with phosphates and water ligands (Krishnamohan Sharma *et al.*, 2003). On the other hand, the complex of Mn^{2+} and polyphosphates in *C. reinhardtii* has been described with high-symmetry octahedral geometry (Tsednee *et al.*, 2019). These findings are in line with the SR-FTIR and EPR results, and imply loose binding of Mn^{2+} to membrane phospholipids and mucilage phosphates in the early stage of the response, and stronger coordination by polyphosphates in the later stage of the response. Metals sequestrated by polyphosphates are typically located within subcellular organelles or granules such as acidocalcisomes (Hong-Hermesdorf *et al.*, 2014). It is noteworthy that the stabilization of the intracellular redox milieu in the later stage may be related to superoxide dismutase-like activity of Mn-polyphosphate complexes (Sharma *et al.*, 2013).

The Fourier transformed EXAFS plot showed much shorter Mn-O bonds in the 72 h sample (Fig. 5F). Surprisingly, FEFF calculation delivered the best fit using parameters of the complex cluster $Mn_{13}Ca_2O_{10}(OH)_2(OMe)_2(O_2CPh)_{18}(H_2O)_4$, which contains two $[Mn_4CaO_5]$ cubane-type clusters (Mishra *et al.*, 2005). One of them is very similar to the structure of OEC tetramanganese-calcium cofactor that catalyzes water oxidation to O_2. All calculated distances between Mn and O (1.876 Å (2 O atoms), 1.937 Å (2 O), 2.203 Å (1 O), 2.329 Å (1 O)), and between two Mn atoms (2.889 Å) in that cluster, match distances in the native OEC (Yano *et al.*, 2005; Zhang *et al.*, 2015). The determined distance between two Mn atoms stems from di-μ-oxido bridged Mn ions (Ruettinger *et al.*, 1997). The presented calculations showed excellent fit with the model according to the previously outlined criteria: distance deviations were < 0.02 Å; differences between sample E_0 and model E_0 were 1.85 eV; reduction factors were 0.777; and Debye-Waller factors were positive and did not overpass departure of 0.01 from the model. The structure of the model complex is mixed-valent and contains Mn^{4+}, $10Mn^{3+}$, and $2Mn^{2+}$. Two Mn_4O_4 cubes are attached to a central, planar Mn_3O_4 unit which also binds two Mn–Ca pairs. Mn^{4+} is in the center, and Mn^{2+} is next to the Ca^{2+} ions (Mishra *et al.*, 2005). It is important to note that the presence of Mn^{2+} in the microalgal cluster may be a result of X-ray-induced photoreduction. This has been reported previously to take place in OEC that was examined by X-rays (Yano *et al.*, 2005). The planar Mn_3O_4 unit accounts for high contribution of this molecule in the linear combination fit of XANES spectrum (Fig. 5D). The similarity between the Mn-O-Ca cluster in *C. sorokiniana* and OEC is supported by voltammetry (Fig. 4B). The reduction and oxidation peak current potentials that were established here (E_{pc} = 155 mV and E_{pa} = 1020 mV), correspond to previously measured potentials for the reduction of Mn^{4+} and oxidation of Mn^{3+} in synthetic OEC cluster (E_{pc} = 83 mV and E_{pa} = 1073 mV, relative to the same reference electrode; a small discrepancy can be explained by the use of different solvents) (Zhang *et al.*, 2015). Finally, it appears that the Mn-O-Ca cluster might be bound to protein(s). FEFF calculations allow the presence of two paths that include C atoms in the second coordination sphere next to O that binds to Mn. The values of the Debye-Waller factor were too large, however, this may be related to the highly disordered environment that is typical for bio-molecules and to the fact that C is a relatively poor X-ray scatterer at the distances where the method become less sensitive and accurate (Bordiga *et al.*, 2013). Analogous to the OEC in PSII, the *C. sorokiniana* Mn-O-Ca cluster determined here may bind to a protein through coordination with O atoms in carboxyl groups in Glu and Asp side-chains.

The accumulation of Mn-O structures has also been observed previously in different microalgae and plants. Chaput and colleagues reported that phototrophs that are tolerant of high Mn concentrations show different strategies in handling Mn excess and form intracellular and extracellular Mn-O deposits that are enriched with P. The mechanisms of formation include superoxide production and pH changes (Chaput *et al.*, 2019). *Desmodesmus* sp. has been shown to accumulate 'biogenic Mn oxides' that can be used for catalysis of oxidative degradation of pollutants (Wang *et al.*, 2017). Another study has found the development of Mn-Ca oxides on the cell walls of macroalgae. The deposit showed weak water splitting/oxygen evolving activity (Schöler *et al.*, 2014). Chernev and colleagues have reported that multi-valent Mn-O structures are formed in extracted thylakoid particles at the lumenal side of PSII by oxidation of Mn^{2+} and stabilization of the oxidized Mn^{3+} and Mn^{4+} ions by di-μ-oxo bridging, in analogy to the light-driven self-assembly process of the Mn_4CaO_5 cluster in OEC (Chernev *et al.*, 2020). It is noteworthy that PSII requires frequent reassembly of the OEC within the protein environment in relation to the damage induced by reactive intermediates (Dasgupta *et al.*, 2008). It is tempting to speculate that the Mn-O-Ca cluster may form

at or close to PSII to serve as replenishment for the reassambly. Mn-induced oxidative burst could promote Mn-O-Ca cluster formation through Mn^{2+} oxidation. As noted, Mn^{2+} may undergo oxidation by a hydroperoxyl radical, which shows pK = 4.88 and therefore is favored at lower pH values (Bielski and Willson, 1985), such as in the thylakoid lumen. Mn^{2+} auto-oxidation in oxygen-rich solutions or photo-oxidation may also take place, if strong chelates are accessible to stabilize the resulting Mn^{3+}, which is unstable and susceptible to disproportionation to Mn^{4+} and Mn^{2+} (Bao and Burnap, 2016). The stabilization of nucleating Mn^{3+} intermediates may be provided by protein side-chains which is followed by cluster growth that does not require further ligating residues (Chernev *et al.*, 2020).

Overview of the process and concluding remarks

Metabolism of Mn in microalgae represents a central issue of photosynthetic activity, ecology of aquatic systems, and even climate dynamics, in relation to the essential role of microalgae in carbon fixation and O_2 and biomass production (Mahowald *et al.*, 2018; Krichen *et al.*, 2019). We have identified three distinctive stages in the interactions of *C. sorokiniana* with Mn excess and revealed the final storage ligand (Fig. 6). In the early stage, environmental Mn^{2+} is bound to phosphate moieties in membrane phospholipids and mucilage. The outer rigid cell wall undergoes structural changes. Redox homeostasis is lost as implicated by pronounced oxidation and lipid peroxidation. Such pro-oxidative changes have been reported previously in microalgae in response to some other metals (Nowicka, 2022). Mn and phosphates are loaded into the cell. These dynamic changes are followed by 'stabilization' in the later stage. Mn is mainly bound as Mn^{2+} to polyphosphates that are probably accumulated within acidocalcisomes. Redox balance is re-established and the damage to lipids is repaired. At this stage, the structure of the inner fibrilar wall is modified. Polyphosphates play an escorting role to the final ligands, as proposed previously (Tsednee *et al.*, 2019; Schmollinger *et al.*, 2021). In the final stage, Mn is inserted into a mixed-valent Mn-O-Ca cluster that is dominated by Mn^{3+}, and that resembles the structure of the OEC. The mechanism of transfer of Mn from polyphosphates to the cluster and the localization of the cluster remain to be determined. The transfer probably relies on chaperone properties of polyphosphates (Xie and Jakob, 2019). Structural and redox similarity between the observed Mn-O-Ca cluster and the OEC in PSII may have important implications for the understanding of the evolution of OEC and PSII, the development of artificial water-splitting catalysts, and the use of microalgae in green synthesis of catalytically/redox active metal clusters. The formation of an OEC-like cluster by microalgae speaks in favour of the hypothesis that a PSII precursor promoted the formation of a large Mn cluster on its surface that further succumbed to evolutionary pressure and spatial limits to give today's OEC (Chernev *et al.*, 2020). This is in contrast to the hypothesis of acquisition and incorporation of a 'ready-made' cluster into a mutant protein (Russell and Hall, 2002).

Finally, it is important to point out the main limitations of this study. They are related to the application of high Mn^{2+} concentration, which was needed in order to meet the detection limits of the X-ray based and other analytical methods. Although the selected Mn concentration is not toxic, it induces stress and an appropriate adaptive response. So the observed steps in Mn acquisition are related to both, obtaining a physiological Mn quota and opportunistic accumulation of Mn, and the adaptation to metal excess. Secondly, Mn was applied in the form of a chloride salt. Although much higher concentrations of Cl^- ions than used in this study (0.8 mM Cl^- in the medium plus 2 mM Cl^- in the Mn solution) have been shown to stimulate mucilage synthesis and membrane reorganization (Shetty *et al.*, 2019), some modest effects of increased concentration of Cl^- ions are possible. Finally,

the interactions were analyzed in early stationary phase cultures and not in the early or midexponential growth phase when the cells are the most metabolically active. We decided to primarily study stationary phase cultures due to the expectation that dynamic metabolic changes and rapid increases in cell numbers may affect measurements during the exponential phase. It is noteworthy, that examination of cultures in the early stationary phase is of particular environmental relevance since this is a stage where biomass could be utilised for metal binding and removal (Yan *et al.*, 2022).

Acknowledgements

The authors are grateful to the Elettra Sincrotrone Trieste management and staff for their cooperation, technical and scientific support, and valuable discussion.

Author contributions

IS and JKP: conceptualization, writing – original draft, supervision. SV, MD, MS, MŽ, GA, TD, BZ, JDL, DS, MO, AM: formal analysis, investigation, writing – review & editing. MŽ, GA, TD, BZ, DS: data curation, methodology.

Conflict of interest

The authors declare that they have no conflict of interest.

Funding

This work is supported by the NATO Science for Peace and Security Programme, Project number G5320, and the Ministry of Education, Science and Technological Development of the Republic of Serbia (Grant No. 451-03-9/2021-14/200053). XAFS measurements were performed in the frame of the project No 20210133 and were supported by ICTP-ELETTRA Users Program.

Data Availability

The data supporting the findings of this study are available from the corresponding author, Ivan Spasojević, upon request.

References

Alejandro S, Höller S, Meier B and Peiter E. 2020. Manganese in plants: From acquisition to subcellular allocation. Frontiers in Plant Science **11**, 300.

Alomar TS, Habila MA, Al Masoud N, Alothman ZA, Sheikh M, Soylak M. 2021. Biomass-derived adsorbent for dispersive solid-phase extraction of Cr(III), Fe(III), Co(II) and Ni(II) from food samples prior to ICP-MS detection. Applied Sciences **11,** 7792.

Balzano S, Sardo A, Blasio M, Chahine TB, Dell'Anno F, Sansone C, Brunet C. 2020. Microalgal metallothioneins and phytochelatins and their potential use in bioremediation. Frontiers in Microbiology **11,** 517.

Bao H, Burnap RL. 2016. Photoactivation: The light-driven assembly of the water oxidation complex of photosystem II. Frontiers in Plant Science **7,** 578.

Battah M, El-Ayoty Y, Abomohra AE, El-Ghany SA, Esmael A. 2015. Effect of Mn2+, Co2+ and H2O2 on biomass and lipids of the green microalga Chlorella vulgaris as a potential candidate for biodiesel production. Annals of Microbiology **65,** 155–162.

Baudelet P, Ricochon G, Linder M, Muniglia L. 2017. A new insight into cell walls of Chlorophyta. Algal Research **25,** 333–371.

Bielski BHJ, Willson RL. 1985. Fast kinetic studies of dioxygen-derived species and their metal complexes [and discussion]. Philosophical Transactions of the Royal Society B: Biological Sciences **311,** 473–482.

Blaby-Haas CE, Merchant SS. 2012. The ins and outs of algal metal transport. Biochimica et Biophysica Acta (BBA) - Molecular Cell Research **1823,** 1531–1552.

Boncheva M, Damien F, Normand V. 2008. Molecular organization of the lipid matrix in intact stratum corneum using ATR-FTIR spectroscopy. Biochimica et Biophysica Acta (BBA) - Biomembranes **1778,** 1344–1355.

Borchman D, Sinha S. 2002. Determination of products of lipid oxidation by infrared spectroscopy. Methods in Molecular Biology **186,** 21–28.

Bordiga S, Groppo E, Agostini G, van Bokhoven JA, Lamberti C. 2013. Reactivity of surface species in heterogeneous catalysts probed by in situ X-ray absorption techniques. Chemical Reviews **113,** 1736–1850.

Chaput DL, Fowler AJ, Seo O, Duhn K, Hansel CM, Santelli CM. 2019. Mn oxide formation by phototrophs: Spatial and temporal patterns, with evidence of an enzymatic superoxide-mediated pathway. Scientific Reports **9,** 18244.

Chernev P, Fischer S, Hoffmann J, *et al*. 2020. Light-driven formation of manganese oxide by today's photosystem II supports evolutionarily ancient manganese-oxidizing photosynthesis. Nature Communications **11,** 6110.

Cotton FA, Wilkinson G, Murillo CA, Bochmann M. 1999. Advanced inorganic chemistry. Hoboken: Wiley Interscience.

Culture Collection of Algae and Protozoa. 2022. **https://www.ccap.ac.uk/media/documents/3N_BBM_V.pdf**

Dai S, Xie Z, Wang B, Yu N, Zhao J, Zhou Y, Hua Y, Tian B. 2021. Dynamic polyphosphate metabolism coordinating with manganese ions defends against oxidative stress in the extreme bacterium *Deinococcus radiodurans*. Applied and Environmental Microbiology **87,** e02785-20.

Dasgupta J, Ananyev GM, Dismukes GC. 2008. Photoassembly of the water-oxidizing complex in photosystem II. Coordination Chemistry Reviews **252,** 347–360.

Derenne A, Claessens T, Conus C, Goormaghtigh E. 2013. Infrared spectroscopy of membrane lipids. In: Roberts GCK Ed. Encyclopedia of biophysics. Berlin: Springer, 1074–1081.

Driver T, Bajhaiya AK, Allwood JW, Goodacre R, Pittman JK, Dean AP. 2015. Metabolic responses of eukaryotic microalgae to environmental stress limit the ability of FT-IR spectroscopy for species identification. Algal Research **11,** 148–155.

Eisenhut M. 2019. Manganese homeostasis in cyanobacteria. Plants (Basel) **9,** 18.

Elboulali A, Akriche S, Rzaigui M. 2013. Bis(2-meth-oxy-benzyl-ammonium) di-aqua-bis-(di-hydrogen diphosphato-κ(2) O,O')manganate(II) dihydrate. Acta Crystallographica Section E Structure Reports Online **69,** m572.

Hanikenne M, Esteves SM, Fanara S, Rouached H. 2021. Coordinated homeostasis of essential mineral nutrients: a focus on iron. Journal of Experimental Botany **72,** 2136–2153.

Hong-Hermesdorf A, Miethke M, Gallaher SD, *et al*. 2014. Subcellular metal imaging identifies dynamic sites of Cu accumulation in Chlamydomonas. Nature Chemical Biology **10,** 1034–1042.

Husberg C, Ryde U. 2013. How are hydrogen bonds modified by metal binding? Journal of Biological Inorganic Chemistry **18,** 499–522.

Kalyanaraman B, Darley-Usmar V, Davies KJ, Dennery PA, Forman HJ, Grisham MB, Mann GE, Moore K, Roberts LJ, Ischiropoulos H. 2012. Measuring reactive oxygen and nitrogen species with fluorescent probes: challenges and limitations. Free Radical Biology and Medicine **52,** 1–6.

Khalifeh F, Salari H, Zamani H. 2022. Mechanism of MnO2 nanorods toxicity in marine microalgae Chlorella sorokiniana during long-term exposure. Marine Environmental Research **179,** 105669.

Khramtsov VV, Yelinova VI, Weiner LM, Berezina TA, Martin VV, Volodarsky LB. 1989. Quantitative determination of SH groups in low- and high-molecular-weight compounds by an electron spin resonance method. Analytical Biochemistry **182,** 58–63.

Krichen E, Rapaport A, Le Floc'h E, Fouilland E. 2019. Demonstration of facilitation between microalgae to face environmental stress. Scientific Reports **9,** 16076.

Krishnamohan Sharma CV, Chusuei CC, Clérac R, Möller T, Dunbar KR, Clearfield A. 2003. Magnetic property studies of manganese-phosphate complexes. Inorganic Chemistry **42,** 8300–8308.

Liu J, Tan K, He L, Qiu Y, Tan W, Guo Y, Wang Z, Sun W. 2018. Effect of limitation of iron and manganese on microalgae growth in fresh water. Microbiology **164,** 1514–1521.

Mahowald NM, Hamilton DS, Mackey KRM, Moore JK, Baker AR, Scanza RA, Zhang Y. 2018. Aerosol trace metal leaching and impacts on marine microorganisms. Nature Communications **9,** 2614.

Malavasi V, Soru S, Cao G. 2020. Extremophile microalgae: the potential for biotechnological application. Journal of Phycology **56,** 559–573.

Martell AE, Hancock RD. 1996. Metal complexes. In: Aqueous solutions modern inorganic chemistry series. New York: Plenum.

Martens H, Stark E. 1991. Extended multiplicative signal correction and spectral interference subtraction: new preprocessing methods for near infrared spectroscopy. Journal of Pharmaceutical and Biomedical Analysis **9,** 625–635.

Min SK, Yoon GH, Joo JH, Sim SJ, Shin HS. 2014. Mechanosensitive physiology of Chlamydomonas reinhardtii under direct membrane distortion. Scientific Reports **4,** 4675.

Mishra A, Wernsdorfer W, Abboud KA, Christou G. 2005. The first high oxidation state manganese–calcium cluster: relevance to the water oxidizing complex of photosynthesis. Chemical Communications **1,** 54–56.

Naveed S, Li C, Lu X, Chen S, Yin B, Zhang C, Ge Y. 2019. Microalgal extracellular polymeric substances and their interactions with metal(loid)s: a review. Critical Reviews in Environmental Science and Technology **49,** 1769–1802.

Nowicka B. 2022. Heavy metal-induced stress in eukaryotic algae-mechanisms of heavy metal toxicity and tolerance with particular emphasis on oxidative stress in exposed cells and the role of antioxidant response. Environmental Science and Pollution Research **29,** 16860–16911.

Oh-hama T, Siebelt F, Furihata K, Seto H, Miyachi S, Ohmori M. 1986. 31P-NMR studies on inorganic polyphosphates in microalgae. Journal of Phycology **22,** 485–490.

Pérez-Pérez ME, Lemaire SD, Crespo JL. 2012. Reactive oxygen species and autophagy in plants and algae. Plant Physiology **160,** 156–164.

Rahman I, Kode A, Biswas SK. 2006. Assay for quantitative determination of glutathione and glutathione disulfide levels using enzymatic recycling method. Nature Protocols **1,** 3159.

Rajpoot R, Srivastava RK, Rani A, Pandey P, Dubey RS. 2021. Manganese-induced oxidative stress ultrastructural changes and proteomics studies in rice plants. Protoplasma **258,** 319–335.

Ravel B, Newville M. 2005. ATHENA ARTEMIS HEPHAESTUS: data analysis for X-ray absorption spectroscopy using IFEFFIT. Journal of Synchrotron Radiation **12,** 537–541.

Rijstenbil JW, Haritonidis S, Malea P, Seferlis M, Wijnholds JA. 1998. Thiol pools and glutathione redox ratios as possible indicators of copper toxicity in the green macroalgae Enteromorpha spp from the Scheldt Estuary (SW Netherlands Belgium) and Thermaikos Gulf (Greece N Aegean Sea). Hydrobiologia **385,** 171–181.

Röllin HB, Nogueira CMCA. 2019. Manganese: Environmental pollution and health effects. In: Nriagu JO, Ed. Encyclopedia of environmental health. Amsterdam: Elsevier BV, 617–629.

Russell B. 1995. Determination of factors limiting enzymatic hydrolysis of the Chlorella sorokiniana cell wall (PhD Dissertation). Gainesville: University of Florida.

Russell MJ, Hall AJ. 2002. From geochemistry to biochemistry: chemiosmotic coupling and transition element clusters in the onset of life and photosynthesis. Geochemical News **113,** 6–12.

Ruettinger WF, Campana C, Dismukes GC. 1997. Synthesis and characterization of Mn4O4L6 complexes with cubane-like core structure: A new class of models of the active site of the photosynthetic water oxidase. Journal of American Chemical Society **119,** 6670-6671.

Schmollinger S, Chen S, Strenkert D, Hui C, Ralle M, Merchant SS. 2021. Single-cell visualization and quantification of trace metals in Chlamydomonas lysosome-related organelles. Proceedings of the National Academy of Sciences **118,** e2026811118.

Schöler A, Zaharieva I, Zimmermann S, Wiechen M, Manke A-M, Kurz P, Plieth C, Dau H. 2014. Biogenic manganese–calcium oxides on the cell walls of the algae Chara corallina: Elemental composition, atomic structure, and water-oxidation catalysis. European Journal of Inorganic Chemistry **2014,** 780-790.

Sharma A, Gaidamakova EK, Matrosova VY, Bennett B, Daly MJ, Hoffman BM. 2013. Responses of Mn2+ speciation in Deinococcus radiodurans and Escherichia coli to radiation by advanced paramagnetic resonance methods. Proceedings of the National Academy of Sciences **110,** 5945–5950.

Shetty P, Gitau MM, Maróti G. 2019. Salinity stress responses and adaptation mechanisms in eukaryotic green microalgae. Cells **8,** 1657.

Sule K, Umbsaar J, Prenner EJ. 2020. Mechanisms of Co Ni and Mn toxicity: From exposure and homeostasis to their interactions with and impact on lipids and biomembranes. Biochimica et Biophysica Acta (BBA) - Biomembranes **1862,** 183250.

Sunda WG, Huntsman SA. 1998. Interactions among Cu^{2+}, Zn^{2+}, and Mn^{2+} in controlling cellular Mn, Zn, and growth rate in the coastal alga *Chlamydomonas*. Limnology and Oceanography **43,** 1055–1064.

Sutak R, Botebol H, Blaiseau PL, Léger T, Bouget FY, Camadro JM, Lesuisse E. 2012. A comparative study of iron uptake mechanisms in marine microalgae: iron binding at the cell surface is a critical step. Plant Physiolology **160,** 2271–2284.

Suwalsky M, Villena F, Sotomayor CP. 2010. Mn2+ exerts stronger structural effects than the Mn-citrate complex on the human erythrocyte membrane and molecular models. Journal of Inorganic Biochemistry **104,** 55–61.

Tsednee M, Castruita M, Salomé PA, *et al*. 2019. Manganese co-localizes with calcium and phosphorus in Chlamydomonas acidocalcisomes and is mobilized in manganese-deficient conditions. Journal of Biological Chemistry **294,** 17626–17641.

Vojvodić S, Danilović Luković J, Zechmann B, Jevtović M, Bogdanović Pristov J, Stanić M, Lizzul AM, Pittman JK, Spasojević I. 2020a. The effects of ionizing radiation on the structure and antioxidative and metal-binding capacity of the cell wall of microalga Chlorella sorokiniana. Chemosphere **260,** 127553.

Vojvodić S, Stanić M, Zechman B, Dučić T, Žižić M, Dimitrijević M, Danilović Luković J, Milenković MR, Pittman JK, Spasojević I. 2020b. Mechanisms of detoxification of high copper concentrations by the microalga Chlorella sorokiniana. Biochemical Journal **477,** 3729–3741.

Wang R, Wang S, Tai Y, Tao R, Dai Y, Guo J, Yang Y, Duan S. 2017. Biogenic manganese oxides generated by green algae Desmodesmus sp. WR1 to improve bisphenol A removal. Journal of Hazardous Materials **339,** 310–319.

Watanabe K, Imase M, Sasaki K, Ohmura N, Saiki H, Tanaka H. 2006. Composition of the sheath produced by the green alga Chlorella sorokiniana. Letters in Applied Microbiology **42,** 538–543.

Wiercigroch E, Szafraniec E, Czamara K, Pacia MZ, Majzner K, Kochan K, Kaczor A, Baranska M, Malek K. 2017. Raman and infrared spectroscopy of carbohydrates: A review. Spectrochimica Acta Part A: Molecular and Biomolecular Spectroscopy **185,** 317–335.

World Health Organization. 2011. Manganese in drinking-water - Background document for development of WHO guidelines for drinking-water quality. Geneve: WHO Press.

Xie L, Jakob U. 2019 Inorganic polyphosphate a multifunctional polyanionic protein scaffold. Journal of Biological Chemistry **294,** 2180–2190.

Yan C, Qu Z, Wang J, Cao L, Han Q. 2022. Microalgal bioremediation of heavy metal pollution in water: Recent advances, challenges, and prospects. Chemosphere **286**, 131870.

Yano J, Pushkar Y, Glatzel P, Lewis A, Sauer K, Messinger J, Bergmann U, Yachandra V. 2005. High-resolution Mn EXAFS of the oxygen-evolving complex in photosystem II: structural implications for the Mn4Ca cluster. Journal of American Chemical Society **127,** 14974–14975.

Zhang ZC, Li RQ, Zhang Y. 2009. Diaqua-bis{[1-hydr-oxy-2-(1H-imidazol-3-ium-1-yl)ethane-1,1-di-yl]bis-(hydrogen phospho-nato)}manganese(II). Acta Crystallographica Section E Structure Reports Online **65,** m1701–m1702.

Zhang C, Chen C, Dong H, Shen JR, Dau H, Zhao J. 2015. A synthetic Mn_4Ca-cluster mimicking the oxygen-evolving center of photosynthesis. Science **348,** 690–693.

Zuppini A, Andreoli C, Baldan B. 2007. Heat stress: an inducer of programmed cell death in Chlorella saccharophila. Plant and Cell Physiology **48,** 1000–1009.

Table 1. Bands that identified by SR-FTIR analysis of untreated (control) or treated (1 mM $MnCl_2$ for 1 h or 24 h) *C. sorokiniana* biomass. Changes in the amplitude and shifts are marked with upward/downward and leftward/rightward arrows. ν_{as} and ν_s – stretching vibrations (asymmetric and symmetric), δ – in-plane bending vibrations; ω – out-of-the-plane bending vibrations.

Control	Mn 1 h	Mn 24 h	Assignment
Carbohydrates and phosphates 'fingerprint' region			
1448	1448	1448↓	δ of CH_2 in carbohydrates
1378	1378	1378↓	ω of CH_2 in carbohydrates
1283	1283	1283	ν_{as} and ν_s of P=O in HPO_4^{2-}
1248	1235→	1248	ν_{as} of P=O in phosphate groups on phospholipids, phosphorylated carbohydrates and proteins
		1184	ν of C-C, C-O
1149	1149	1149↑	ν_s of C-C, C-O, C-O-C and C-O-P in carbohydrates
1072	1072	1072↑	ν_s of C-C, C-O, C-O-C and C-O-P in carbohydrates
1044	1044	1044	ν_{as} of P=O in HPO_4^{2-}
1028	1028↑	1030←	ν_s of C-C, C-O, C-O-C and C-O-P in carbohydrates
		940	ν_{as} of C-C, C-O
Proteins 'fingerprint' region			
1734	1734	1734	ν of C=O
1644	1647←	1648←	ν of C=O···H-N in primary amides
1535	1535	1535	δ of N–H in secondary amides
Lipids 'fingerprint' region			
3002	3004↓←	3004↓←	ν of C–H in C=C–H in unsaturated fatty acids
2950	2950↑	2950	ν_{as} of CH_3 in fatty acids
2912	2916↑←	2912↑	ν_{as} of CH_2 in fatty acids
2868	2868	2868↑	ν_s of CH_3 in fatty acids
2847	2849←	2847↑	ν_s of CH_2 in fatty acids

Figure legends

Fig. 1. *C. sorokiniana* culture growth parameters and the impact of Mn. (A) Growth curve determined by optical density at 750 nm (OD_{750}) measurements for 30 days. The data were fitted using sigmoidal fit (R^2 = 0.990). Arrows show time points of treatment in the exponential phase (day 7; pale arrow), and early stationary/late exponential phase (day 20; dark arrow). (B) Changes in OD_{750} during a 7 day period for cultures that were untreated or treated with different $MnCl_2$ concentrations at day 7. (C) Changes in OD_{750} during a 7 day period for cultures that were untreated or treated with different $MnCl_2$ concentrations at day 20. (D) Biomass of cultures that were untreated or treated with different $MnCl_2$ concentrations at day 20. (E) Comparison of Mn accumulation in the biomass after 24 h treatment with 1 mM $MnCl_2$ at day 7 and day 20. (F) Viability of the untreated culture cells in stationary phase, from day 20 to day 27. Data are presented as means ± SE. Significance compared to values for the same cultures at day 7 or day 20 was determined using Mann–Whitney 2-tailed test (*$p < 0.05$).

Fig. 2. Structural and mineral nutrient accumulation analysis of *C. sorokiniana* cells that were untreated (control) or treated with 1 mM $MnCl_2$. (A) SEM micrographs. Mucilage can be observed as flakes (arrows) that cover cells in treated samples at 1 h and 24 h time points. White circles and boxes indicate the areas where EDS data were collected. Bars = 5 µm. (B) Atomic fraction of different elements in microalgal biomass (means ± SE), as determined by EDS. (C) Mn, P, Fe and Zn accumulation profiles over time in Mn treated biomass (means ± SE), as determined by ICP-AES. Different letters mark statistical difference ($p < 0.05$), according to one-way ANOVA followed by Duncan's *post hoc* test. b.d.l. – below detection limit. (D) SR-FTIR spectral 'fingerprint' region for carbohydrates, phosphates, and nucleic acids. (E) SR-FTIR 'fingerprint' region for proteins and carbonyl groups. (F) SR-FTIR 'fingerprint' region for lipids. All treatments were initiated at day 20. Wavenumbers for bands in control samples are presented.

Fig. 3. Redox changes in *C. sorokiniana* cells in response to 1 mM $MnCl_2$ addition over 24 h. (A) Fluorescence intensity of DCF (arbitrary units – a.u.) that is proportional to intracellular ROS level. (B) Intracellular concentration of reduced thiols that were determined by EPR and RSSR spin-probe. *-statistically significant ($p < 0.05$) compared to the initial value (at 0 h). (C) Total concentration of glutathione (reduced + oxidized) in microalgal cells. All data are presented as mean values ± SE. (D) Lipid peroxidation-related parameters are the intensity of C=C band and the ratio of CH_2 and CH_3 bands intensities. Boxes represent the median and the 25^{th} and 75^{th} percentiles; whiskers represent the non-outlier range; circles represent outliers. Different letters mark statistical difference ($p < 0.05$), according to one-way ANOVA followed by Duncan's *post hoc* test. All treatments were initiated at day 20.

Fig. 4. The analysis of changes in the redox form and coordination of Mn. (A) EPR spectra of biomass of *C. sorokiniana* culture that was untreated (control), or exposed to 1 mM $MnCl_2$ then measured at 1 h or 24 h time points. Prior to freeze-drying, cells were washed with H_2O (to remove Mn^{2+} from the solution; dark lines), or with EDTA (to remove Mn^{2+} from the cell surface; pale lines). Mean values (± SE) of amplitude of the first line in six-line Mn^{2+} signal that was normalized to sample mass, are presented.

Peak at g = 2.005 is assigned to an organic radical. (B) Cyclic voltammograms of Mn in 5% nitric acid (v/v) extracts of biomass of microalgae that were treated with 1 mM $MnCl_2$ then examined at 1 h, 24 h, and 48 h time points. All treatments were initiated at day 20. (C) Solutions (1 mM) of $MnCl_2$, Mn_2O_3, MnO_2, and $KMnO_4$ that were used as standards for Mn^{2+}, Mn^{3+}, Mn^{4+}, and Mn^{7+}. Oxidation/anodic (E_{pa}) and reduction/cathodic peak current potentials (E_{pc}) are labeled.

Fig. 5. XANES and EXAFS analysis of Mn in the biomass from *C. sorokiniana* cultures that were exposed to 1 mM $MnCl_2$ then examined at 1 h, 24 h or 72 h time points. (A) XANES spectra of Mn in *C. sorokiniana* at different times after treatment. (B) Comparison of XANES spectra of Mn in *C. sorokiniana* at 1 h and 24 h after Mn treatment, with the spectrum of Mn-acetate and $MnCl_2$. (C) Pre-edge region of XANES spectra of Mn in *C. sorokiniana* at 1 h and 24 h after Mn treatment. (D) Linear combination fit of XANES spectrum of Mn in *C. sorokiniana* at 72 h after Mn treatment (goodness of the fit was R = 0.002). Spectra of Mn^{2+}, Mn^{3+} and Mn^{4+} standard compounds are presented at intensities that were used in the fit. (E) The first derivatives of XANES spectra of Mn in *C. sorokiniana* at 72 h and the standard compounds (Mn-acetate, Mn_2O_3, and MnO_2). (F) Fourier transformed EXAFS spectra of Mn in *C. sorokiniana* biomass and corresponding fits (dotted lines). All treatments were initiated at day 20.

Fig. 6. The proposed stages of the response of *C. sorokiniana* to increased environmental Mn^{2+}. Early stage: Mn is mainly bound as Mn^{2+} to phosphate moieties in membrane phospholipids and released mucilage. Mn and phosphates are accumulated in the cell. Mn^{2+} enter the cells to induce increased ROS production which is accompanied by lipid peroxidation (LP) and decreased levels of reduced thiols (R-SH) and total glutathione (GSH). Outer cell wall undergoes restructuration. Later stage: Mn is mainly bound as Mn^{2+} to polyphosphates. ROS, R-SH and GSH levels are stabilized. Lipid peroxidation is repaired. The structure of the inner cell wall is altered. Final stage: The influx of Mn and phosphates is continued. Mn is stored in mixed-valent deposits with Mn^{4+}, Mn^{3+}, Mn^{2+} that are coordinated with O and Ca^{2+} and that contain [Mn_4CaO_5] cubane-type cluster (part of the hypothetical structure is illustrated).

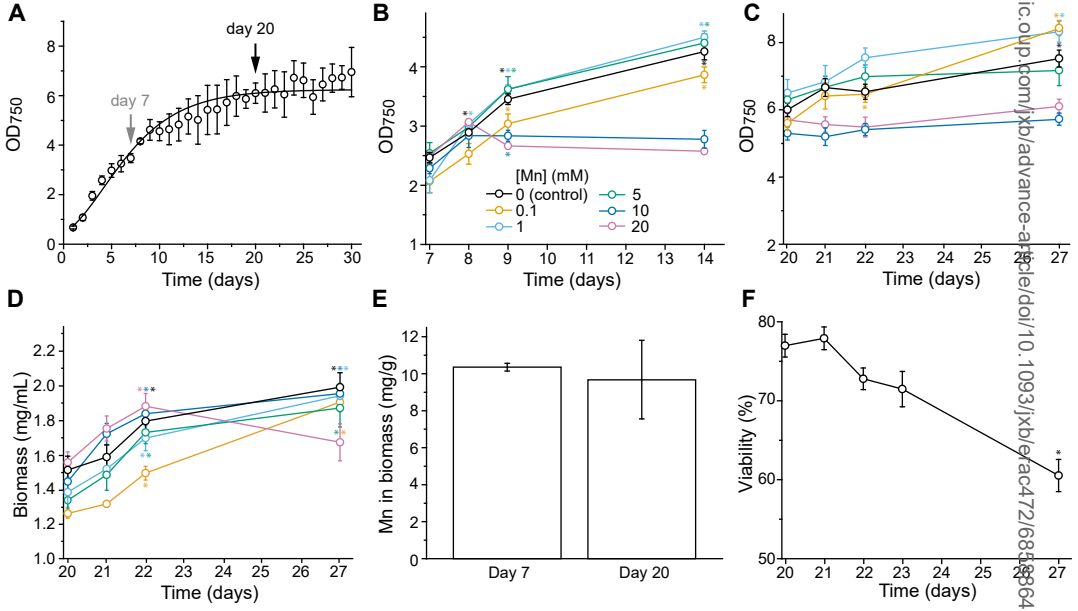

Fig. 1. *C. sorokiniana* culture growth parameters and the impact of Mn. (A) Growth curve determined by optical density at 750 nm (OD_{750}) measurements for 30 days. The data were fitted using sigmoidal fit ($R^2 = 0.990$). Arrows show time points of treatment in the exponential phase (day 7; pale arrow), and early stationary/late exponential phase (day 20; dark arrow). (B) Changes in OD_{750} during a 7 day period for cultures that were untreated or treated with different $MnCl_2$ concentrations at day 7. (C) Changes in OD750 during a 7 day period for cultures that were untreated or treated with different $MnCl_2$ concentrations at day 20. (D) Biomass of cultures that were untreated or treated with different $MnCl_2$ concentrations at day 20. (E) Comparison of Mn accumulation in the biomass after 24 h treatment with 1 mM $MnCl_2$ at day 7 and day 20. (F) Viability of the untreated culture cells in stationary phase, from day 20 to day 27. Data are presented as means ± SE. Significance compared to values for the same cultures at day 7 or day 20 was determined using Mann–Whitney 2-tailed test (*p < 0.05).

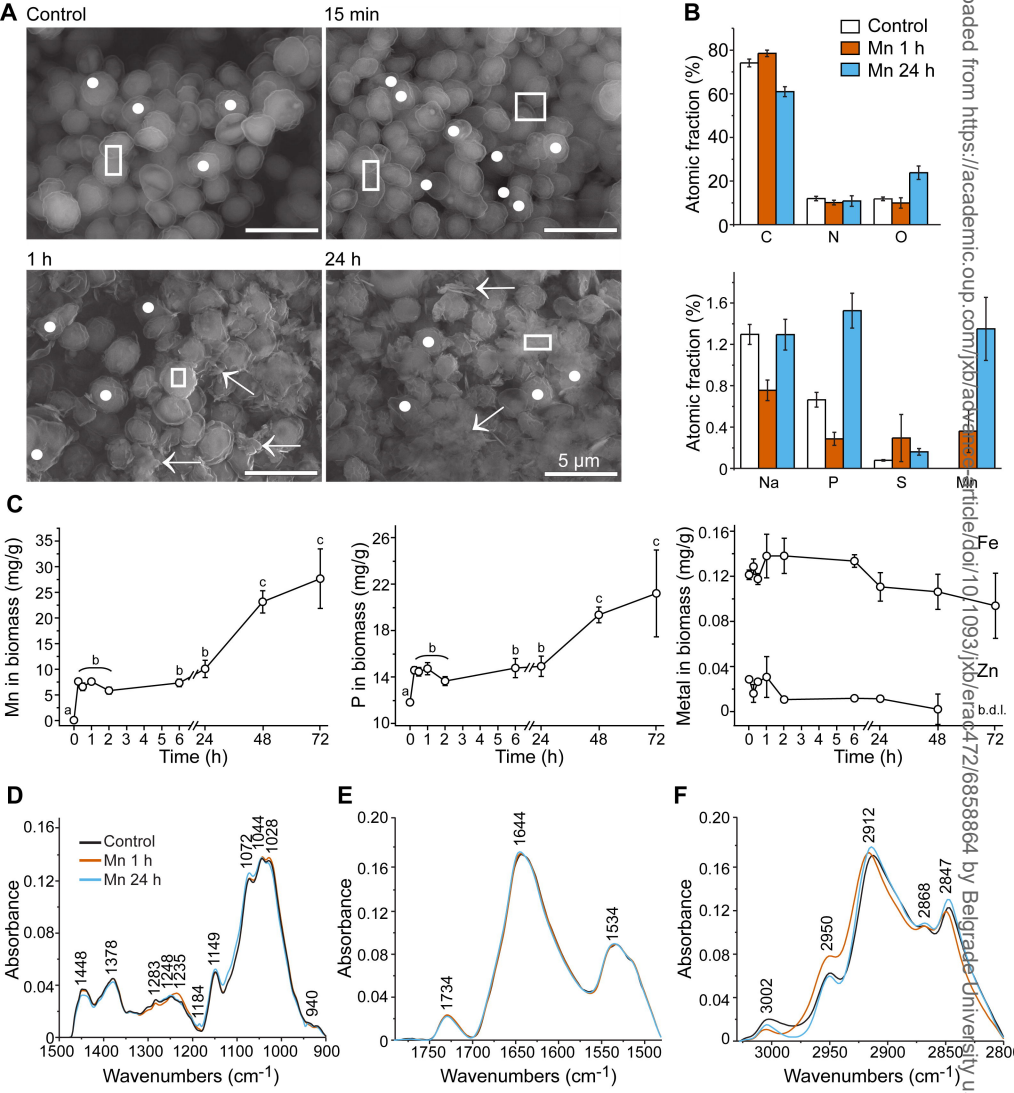

Fig. 2. Structural and mineral nutrient accumulation analysis of *C. sorokiniana* cells that were untreated (control) or treated with 1 mM $MnCl_2$. (A) SEM micrographs. Mucilage can be observed as flakes (arrows) that cover cells in treated samples at 1 h and 24 h time points. White circles and boxes indicate the areas where EDS data were collected. Bars = 5 µm. (B) Atomic fraction of different elements in microalgal biomass (means ± SE), as determined by EDS. (C) Mn, P, Fe and Zn accumulation profiles over time in Mn treated biomass (means ± SE), as determined by ICP-AES. Different letters mark statistical difference ($p < 0.05$), according to one-way ANOVA followed by Duncan's *post hoc* test. b.d.l. – below detection limit. (D) SR-FTIR spectral 'fingerprint' region for carbohydrates, phosphates, and nucleic acids. (E) SR-FTIR 'fingerprint' region for proteins and carbonyl groups. (F) SR-FTIR 'fingerprint' region for lipids. All treatments were initiated at day 20. Wavenumbers for bands in control samples are presented.

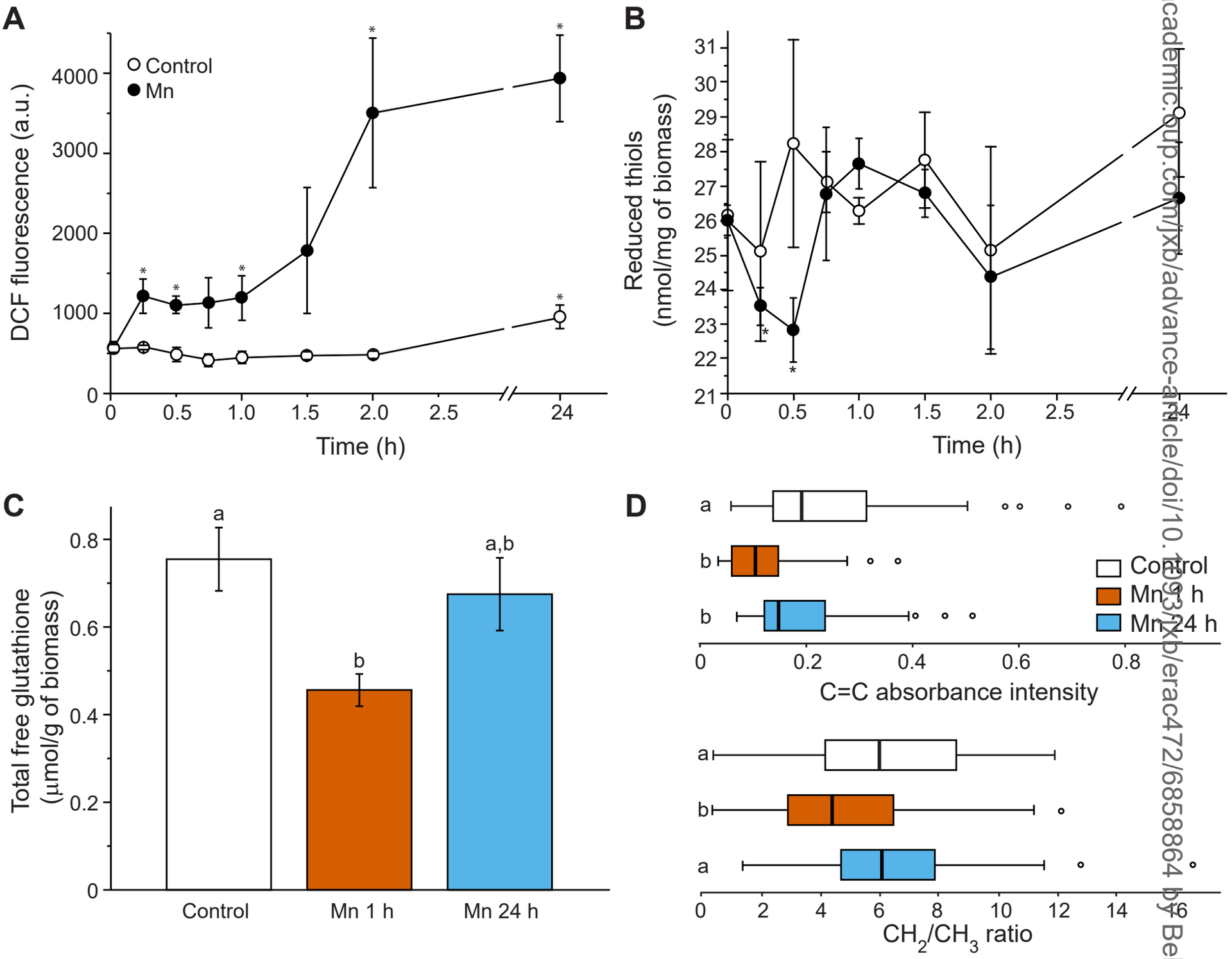

Fig. 3. Redox changes in *C. sorokiniana* cells in response to 1 mM $MnCl_2$ addition over 24 h. (A) Fluorescence intensity of DCF (arbitrary units – a.u.) that is proportional to intracellular ROS level. (B) Intracellular concentration of reduced thiols that were determined by EPR and RSSR spin-probe. *- statistically significant ($p < 0.05$) compared to the initial value (at 0 h). (C) Total concentration of glutathione (reduced + oxidized) in microalgal cells. All data are presented as mean values ± SE. (D) Lipid peroxidation-related parameters are the intensity of C=C band and the ratio of CH_2 and CH_3 bands intensities. Boxes represent the median and the 25th and 75th percentiles; whiskers represent the non-outlier range; circles represent outliers. Different letters mark statistical difference ($p < 0.05$), according to one-way ANOVA followed by Duncan's *post hoc* test. All treatments were initiated at day 20.

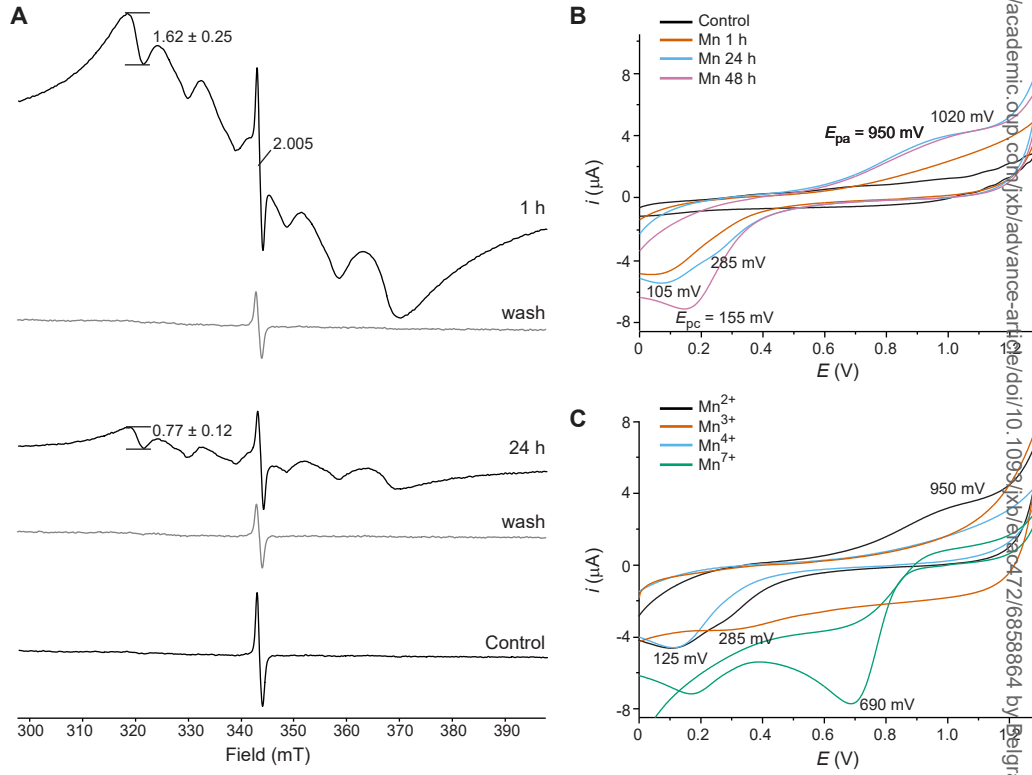

Fig. 4. The analysis of changes in the redox form and coordination of Mn. (A) EPR spectra of biomass of *C. sorokiniana* culture that was untreated (control), or exposed to 1 mM $MnCl_2$ then measured at 1 h or 24 h time points. Prior to freeze-drying, cells were washed with H_2O (to remove Mn^{2+} from the solution; dark lines), or with EDTA (to remove Mn^{2+} from the cell surface; pale lines). Mean values (± SE) of amplitude of the first line in six-line Mn^{2+} signal that was normalized to sample mass, are presented. Peak at g = 2.005 is assigned to an organic radical. (B) Cyclic voltammograms of Mn in 5% nitric acid (v/v) extracts of biomass of microalgae that were treated with 1 mM $MnCl_2$ then examined at 1 h, 24 h, and 48 h time points. All treatments were initiated at day 20. (C) Solutions (1 mM) of $MnCl_2$, Mn_2O_3, MnO_2, and $KMnO_4$ that were used as standards for Mn^{2+}, Mn^{3+}, Mn^{4+}, and Mn^{7+}. Oxidation/anodic (E_{pa}) and reduction/cathodic peak current potentials (E_{pc}) are labeled.

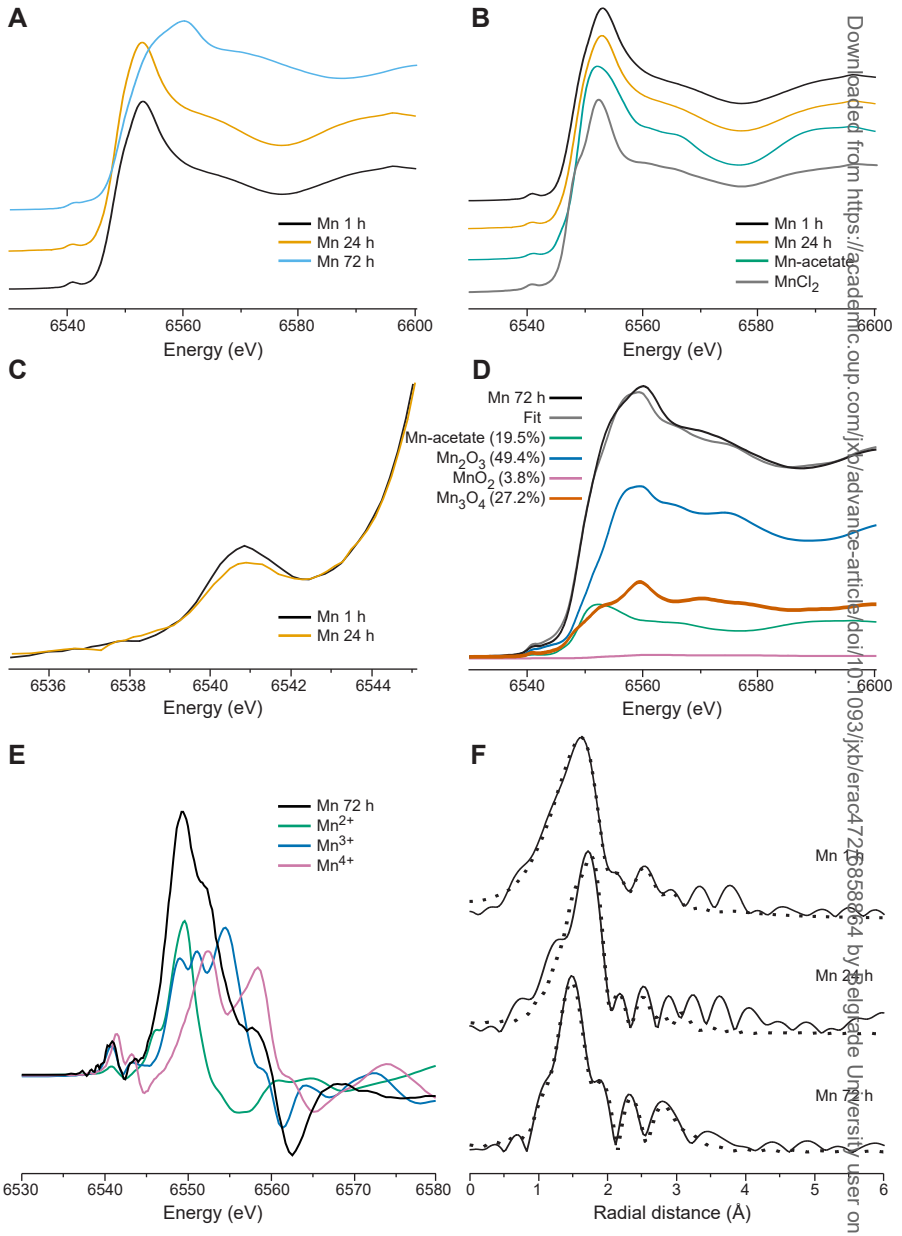

Fig. 5. XANES and EXAFS analysis of Mn in the biomass from *C. sorokiniana* cultures that were exposed to 1 mM $MnCl_2$ then examined at 1 h, 24 h or 72 h time points. (A) XANES spectra of Mn in *C. sorokiniana* at different times after treatment. (B) Comparison of XANES spectra of Mn in *C. sorokiniana* at 1 h and 24 h after Mn treatment, with the spectrum of Mn-acetate and MnCl2. (C) Pre-edge region of XANES spectra of Mn in *C. sorokiniana* at 1 h and 24 h after Mn treatment. (D) Linear combination fit of XANES spectrum of Mn in *C. sorokiniana* at 72 h after Mn treatment (goodness of the fit was $R = 0.002$). Spectra of Mn^{2+}, Mn^{3+} and Mn^{4+} standard compounds are presented at intensities that were used in the fit. (E) The first derivatives of XANES spectra of Mn in *C. sorokiniana* at 72 h and the standard compounds (Mn-acetate, Mn_2O_3, and MnO_2). (F) Fourier transformed EXAFS spectra of Mn in *C. sorokiniana* biomass and corresponding fits (dotted lines). All treatments were initiated at day 20.

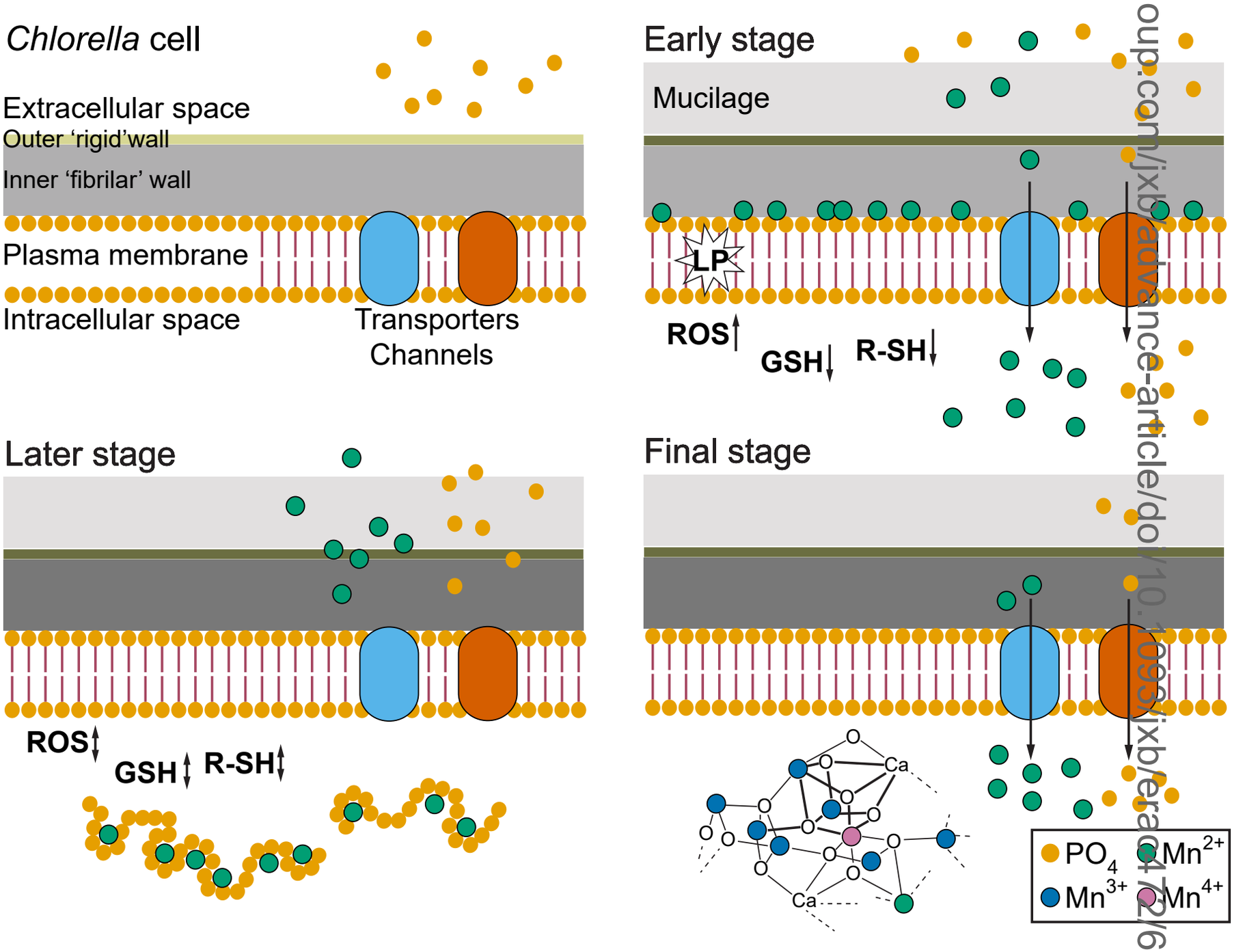

Fig. 6. The proposed stages of the response of *C. sorokiniana* to increased environmental Mn^{2+}. Early stage: Mn is mainly bound as Mn^{2+} to phosphate moieties in membrane phospholipids and released mucilage. Mn and phosphates are accumulated in the cell. Mn^{2+} enter the cells to induce increased ROS production which is accompanied by lipid peroxidation (LP) and decreased levels of reduced thiols (R-SH) and total glutathione (GSH). Outer cell wall undergoes restructuration. Later stage: Mn is mainly bound as Mn^{2+} to polyphosphates. ROS, R-SH and GSH levels are stabilized. Lipid peroxidation is repaired. The structure of the inner cell wall is altered. Final stage: The influx of Mn and phosphates is continued. Mn is stored in mixed-valent deposits with Mn^{4+}, Mn^{3+}, Mn^{2+} that are coordinated with O and Ca^{2+} and that contain $[Mn_4CaO_5]$ cubane-type cluster (part of the hypothetical structure is illustrated).